Impact of Controller Saturation on Instability Behavior of Grid-Connected Inverters

Xuehua Wang, *Member, IEEE*, Yuying He, *Member, IEEE*, Kuang Qin, Hao Zhang, *Student Member, IEEE*, Donghua Pan, *Member, IEEE*, Xinbo Ruan, *Fellow, IEEE*, Qingfeng Zhou, and Chuan Yao

***Abstract*—For the power-electronics-based power system, a kind of stable operation with constant-amplitude oscillation was often witnessed in the reported instability incidents. In some cases, the root is proved to be negative damping by the theoretical analysis based on the linear model and the impedance-based stability theory. However, the negative damped resonances should diverge. This leaves a void why the analysis result is not in accord with the field measurement. This article aims to provide a potential answer for the disaccord, i.e., the controller saturation which is commonly ignored in the modeling process due to its nonlinearity. The controller saturation is linearized by the describing function and the improved linear model is developed. By applying the generalized Nyquist stability criterion, the impact of the controller saturation on the instability behavior of grid-connected inverters is identified, which reveals the underlying mechanism of the constant-amplitude oscillation. The theoretical expectations are finally validated by the experimental results.**

***Index Terms*—Constant-amplitude oscillation, controller saturation, describing function, grid-connected inverter, stability.**

I. Introduction

DRIVEN by the large-scale utilization of renewable energies, power-electronics-based power systems have been spread worldwide in recent years [1]. The grid-connected inverters, as effective interfaces between the renewable energy plant and the power grid, exhibit superior features including the controllability, sustainability, scalability, and high efficiency [2], [3]. On the other hand, they also face new challenges, such as the wideband instability caused by the inverter-grid interactions [4], [5].

A number of unidentified instability incidents have been frequently reported due to the inverter-grid interaction [6]–[12]. For example, in 1995, the first interaction resonance was witnessed in a railway traction in Swiss [10]. In 2013, oscillation of several hundred hertz happened in an islanded offshore grid in Germany [11]. In 2017, oscillation with the resonant frequency of 1.27 kHz was witnessed in Luxi high voltage direct current transmission system in China [12]. The instability phenomena in these incidents can be concluded as follows [13].

1) These instability phenomena arise over a wide frequency range, from several hertz to multiple kilohertz, and the resonant frequency bears no relation to the conventional harmonics (i.e., integer multiples of the fundamental frequency).
2) In some cases, the oscillations diverge, which eventually triggers protection or leads to physical damage. Yet, some oscillations do not diverge, which features stable operation with constant-amplitude oscillation. It may vanish over time, last for hours or even permanently.

Great efforts have been made to identify the root causes of these different instability behaviors [14]–[18]. Two analytical methods were commonly adopted for the stability analysis [19], namely the eigenvalue analysis [20] and the impedance-based stability analysis [21]. Essentially, these two methods are both developed from the small-signal model, and they are performed in the time domain and the frequency domain, respectively. Comparatively, the latter is more convenient since it greatly alleviates the computation burden and can be applied without the prior knowledge of the grid configuration [22]–[25].

For the impedance-based stability method, the assessment of system stability is based on the ratio of the grid impedance and the inverter output impedance [22]. Accordingly, the level of damped (i.e., negative-damped, underdamped, critically damped, or overdamped) resonance can be determined. The classical linear control theory tells that the negative-damped resonance ought to be divergent [26]. However, as reported previously, plenty of the negative-damped resonances, in practice, were witnessed as constant-amplitude oscillations and remain stable over time. So, two questions come to mind naturally: Why does not the theoretical analyses coincide with the observations

Manuscript received September 12, 2021; revised December 3, 2021; accepted January 15, 2022. Date of publication January 27, 2022; date of current version March 24, 2022. This work was supported by the Opening Foundation of State Key Laboratory of HVDC, CSG Electric Power Research Institute, under Grant SKLHVDC-2021-KF-08. Recommended for publication by Associate Editor M. Molinas. *(Corresponding author: Yuying He.)*

Xuehua Wang, Yuying He, and Hao Zhang are with the State Key Laboratory of Advanced Electromagnetic Engineering and Technology, School of Electrical and Electronic Engineering, Huazhong University of Science and Technology, Wuhan 430074, China (e-mail: wang.xh@hust.edu.cn; heyuying@hust.edu.cn; zhangh98@hust.edu.cn).

Kuang Qin is with the State Grid Hunan Electric Power Company Limited Economic and Technical Research Institute, Changsha 410004, China (e-mail: chaserqk@hust.edu.cn).

Donghua Pan is with the Holding Company of China State Shipbuilding Corporation, Wuhan 430064, China (e-mail: pan.dh@outlook.com).

Chuan Yao is with the Wuhan Second Ship Design and Research Institute, Wuhan 430064, China (e-mail: yaochuan_hbwh@163.com).

Xinbo Ruan is with the Center for More-Electric-Aircraft Power Systems, College of Automation Engineering, Nanjing University of Aeronautics and Astronautics, Nanjing 210016, China (e-mail: ruanxb@nuaa.edu.cn).

Qingfeng Zhou is with NR Electric Company, Ltd., Nanjing 211102, China (e-mail: zhouqingfeng@nrec.com).

Color versions of one or more figures in this article are available at https://doi.org/10.1109/TPEL.2022.3146619.

Digital Object Identifier 10.1109/TPEL.2022.3146619

from field measurement? and how to accurately interpret the system instability behavior? These two questions are not clarified so far, which will be answered in this article.

In fact, some inconspicuous factors were generally ignored when establishing the small-signal model, and they are suspected to be the root causes of the difference between the theory and practice. For example, a controller saturation is usually employed to prevent the overflow of the controller output [27], [28], i.e., limiting the maximum duty cycle. Yet, it is generally omitted in the conventional modeling process [29]. In principle, when the controller output reaches saturation, nonlinear modulation will occur, resulting in abundant harmonics in the plant output, i.e., the grid current. In other words, the nonlinear characteristic is featured by the saturation process, making the conventional linear modeling and stability analysis insufficient. Meanwhile, due to the nonlinear characteristic, the small-signal modeling with consideration of the controller saturation is tough [30].

The describing function method is an effective tool for analyzing nonlinear systems, which was used to study the power filter [31], photovoltaic generators [32], [33], the half-bridge converter [34], etc. For example, this method was applied to estimate the nonlinear inductance for large power filter design in [31] and reveal the effects of inductor's nonlinear behavior on the performance of current controllers in [32]. So, the describing function will be used in our work to unfold the impact mechanism of the nonlinear controller saturation on the instability behavior of the grid-connected inverter. First, an improved linear model with consideration of the controller saturation will be developed with the describing function. Then, with the improved model, the mechanism of the impact of the controller saturation on the instability oscillation will be clarified.

The rest of this article is organized as follows. In Section II, a brief description of the *LCL*-type grid-connected inverter is presented. The conventional linear model is reviewed and its limitation on the stability assessment is identified in Section III. In Section IV, the describing function is used to linearize the controller saturation, and the generalized Nyquist stability criterion is elaborated for accurate stability assessment. In Section V, the impact mechanism of the controller saturation on the instability behavior of the *LCL*-type grid-connected inverter is clearly illustrated. In Section VI, the theoretical expectations are confirmed by the experimental results. Finally, Section VII concludes this article.

II. System Description

Fig. 1 shows the configuration of a single-phase full-bridge voltage-source inverter connected to the power grid through an *LCL* filter, where L_1, C, and L_2 are the inverter-side inductor, filter capacitor, and grid-side inductor, respectively. The power grid at the point of common coupling (PCC) is modeled by the Thevenin equivalent circuit, consisting of an ideal voltage source v_g in series with a grid impedance Z_g.

The primary control objective is to shape the grid current i_g to be sinusoidal and keep it in phase with the PCC voltage $v_{\rm PCC}$. For this purpose, a phase-locked loop is used to extract the phase of $v_{\rm PCC}$. Then, combining the extracted result θ with a demanded

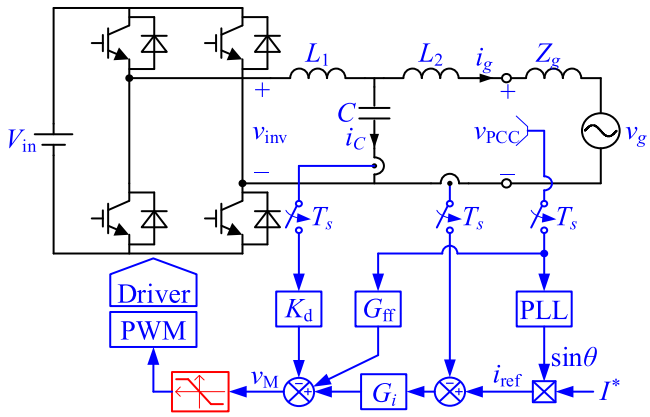

Fig. 1. Configuration of the single-phase *LCL*-type grid-connected inverter.

current amplitude I^* forms the current reference $i_{\rm ref}$. The grid current i_g is regulated to track $i_{\rm ref}$ by a current regulator G_i. To damp the *LCL* resonance, the capacitor-current-feedback active damping is adopted, and K_d is the damping gain. In practice, noticeable background harmonics exist in $v_{\rm PCC}$, which tends to distort i_g. To mitigate this adverse effect, a PCC voltage feedforward with the function of $G_{\rm ff}$ is adopted [12]. Summing up the outputs of G_i, $G_{\rm ff}$ and the sensed damping term i_C, yields the modulation signal v_M. Via the controller saturation and the digital pulsewidth modulation, the control signals of the power switches are generated.

It is worth noting that the controller saturation is responsible for limiting the maximum duty cycle. When v_M does not exceed its limits, the modulation is linear, and the duty cycle varies sinusoidal. Otherwise, the nonlinear modulation occurs, and the associated duty cycle is clamped to its maximal value.

III. Limitation of the Conventional Linear Model

A. Impedance-Based Stability Analysis

Fig. 2(a) shows the block diagram of the grid-connected inverter, where $G_{\rm d}(s)$ represents the time delay and is commonly approximated as

$$G_{\rm d}(s) = e^{-1.5sT_s} \tag{1}$$

with T_s being the sampling period.

In the classical linear control theory, the controller saturation is commonly neglected when assessing the stability of the grid-connected system. In common, the impedance-based stability analysis method is applied, which depends on

$$i_g(s) = i_o(s) - \frac{v_{\rm PCC}(s)}{Z_o(s)} \tag{2}$$

where i_o is the equivalent current source resulted from $i_{\rm ref}$, and Z_o is the output impedance of the inverter, expressed as

$$\begin{aligned} Z_o(s) &\triangleq -\frac{v_{\rm PCC}(s)}{i_g(s)} \\ &= L_2 \frac{s^3 + G_{\rm d}\left(s^2 K_{\rm d} + G_i/(L_2C)\right)/L_1 + s\omega_r^2}{s^2 + sK_{\rm d}G_{\rm d}/L_1 + (1 - G_{\rm d}G_{\rm ff})/(L_1C)} \end{aligned} \tag{3}$$

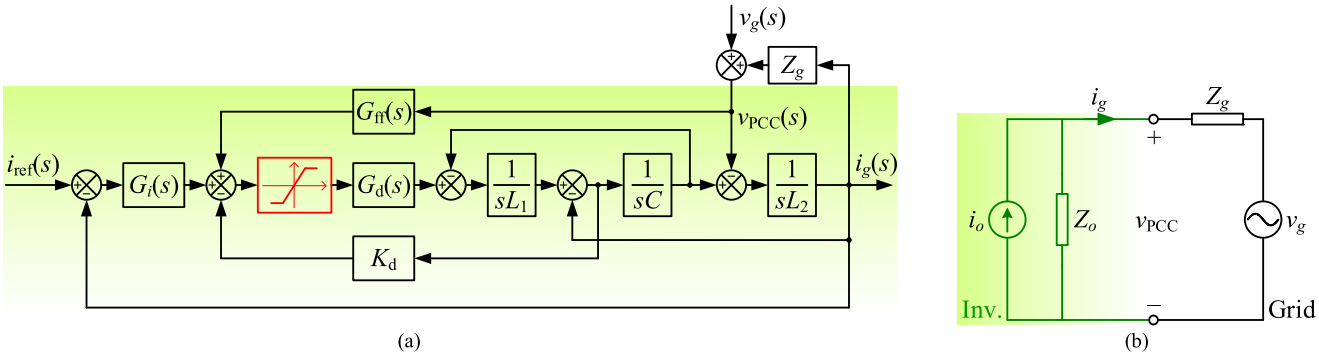

Fig. 2. Modeling of the *LCL*-type grid-connected inverter. (a) Block diagram. (b) Norton equivalent circuit.

where ω_r is the *LCL* resonant frequency, expressed as

$$\omega_r = 2\pi f_r = \sqrt{\frac{L_1 + L_2}{L_1 L_2 C}}. \tag{4}$$

Equation (2) tells that i_g consists of two parts. One is i_o, which reflects the tracking ability of the inverter. The other is $v_{\rm PCC}(s)/Z_o(s)$, which reflects the disturbance rejection ability of the inverter. According to (2), the grid-connected inverter can be modeled by a Norton equivalent circuit, consisting of a current source i_o in parallel with the output impedance Z_o, as shown in Fig. 2(b), and the grid current i_g can be further rewritten as

$$i_g(s) = \left(i_o(s) - \frac{v_g(s)}{Z_o(s)}\right) \cdot \frac{1}{1 + Z_g(s)/Z_o(s)}. \tag{5}$$

As shown in (5), the system stability can be elaborated from the multiplied two terms.

1) $i_o(s) - v_g(s)/Z_o(s)$: This term represents the stability under $Z_g = 0$, which is certainly ensured in the controller design process.
2) $1/(1+Z_g(s)/Z_o(s))$: This term is related to Z_g, determining the dynamic inverter-grid interaction. It generally resembles a minor loop whose gain is Z_g/Z_o, and the stability is assessed by the phase margin PM, i.e.,

$$\text{PM} = 180^\circ - [\angle Z_g(j\omega_{\rm int}) - \angle Z_o(j\omega_{\rm int})] \tag{6}$$

where $\omega_{\rm int} = 2\pi f_{\rm int}$ is the intersection frequency of Z_g and Z_o in the magnitude plot.

Since the practical power grid is generally inductive, the worst case $\angle Z_g = 90^\circ$ is considered, i.e., $Z_g = sL_g$, where L_g is the grid inductance, which results in PM $= 90^\circ + \angle Z_o(j\omega_{\rm int})$. Accordingly, no matter how weak grid is connected, as long as $\angle Z_o(j\omega_{\rm int}) > -90^\circ$, PM $> 0^\circ$ will be guaranteed, and the inverter would operate stably under the weak grid.

To eliminate the adverse effect of $v_{\rm PCC}$ on i_g, the magnitude of Z_o is expected as high as possible. Ideally, it is preferably infinite by tuning $G_{\rm ff}$ as [4]

$$G_{\rm ff\_ideal}(s) = \frac{1}{G_{\rm d}(s)} + sK_{\rm d}C + s^2 L_1 C \cdot \frac{1}{G_{\rm d}(s)} \tag{7}$$

where $G_{\rm ff\_ideal}(s)$ is the ideal full-feedforward function.

As shown in (7), a pure prediction component $1/G_{\rm d}(s)$ exists in the first and third terms. In practice, it cannot be realized physically, and thus is commonly discarded, giving rise to the practical full-feedforward function [35], i.e.,

$$G_{\rm ff0}(s) = 1 + sK_{\rm d}C + s^2 L_1 C \tag{8}$$

which consists of three feedforward elements, i.e., the proportional, derivative, and second-derivative elements.

Note that the derivative part should be properly discretized in the digital control. Among the typical discretization methods, the Backward Euler is widely used [36], expressed as

$$s = (z-1)/(zT_s). \tag{9}$$

For convenience of illustrating in s domain, substituting (9) into (8), and inversely considering $z = e^{sTs}$, yields

$$G_{\rm ff}(s) = 1 + \frac{e^{sT_s} - 1}{e^{sT_s} T_s} K_{\rm d} C + \left(\frac{e^{sT_s} - 1}{e^{sT_s} T_s}\right)^2 L_1 C \tag{10}$$

The $G_{\rm ff}$ shown in (10) is the practical discretized full-feedforward function expressed in s domain.

By substituting the prototype parameters given in Table I in Section VI into (3), the Bode diagrams of the resultant output impedance $Z_{o\_\rm ff}$ are depicted in Fig. 3. As shown, the unexpected result $\angle Z_{o\_\rm ff} < -90^\circ$ occurs in two frequency bands (0, f_1) and (f_2, f_3), where $f_1 \approx 600$ Hz, $f_2 \approx 1.6$ kHz, and $f_3 \approx 3.2$ kHz and they are the boundary frequencies leading to $\angle Z_{o\_\rm ff} = -90^\circ$. Once the intersection frequency $f_{\rm int}$ falls in these two frequency bands, PM $> 0^\circ$ is not satisfied [see (6)] and thus

TABLE I
PARAMETERS OF THE PROTOTYPE

Parameters	Symbols	Values	Parameters	Symbols	Values
Input voltage	$V_{\rm in}$	360 V	Inv.-side inductor	L_1	600μH
Grid voltage	V_g	220 V	Filter capacitor	C	10 μF
Output power	P_o	6 kW	Grid-side inductor	L_2	150 μH
Switching frequency	f_{sw}	10 kHz	Damping gain	$K_{\rm d}$	1.97
Sampling frequency	f_s	20 kHz	Proportional coefficient	K_p	4.7
Line frequency	f_o	50 Hz	Integral coefficient	K_i	7250

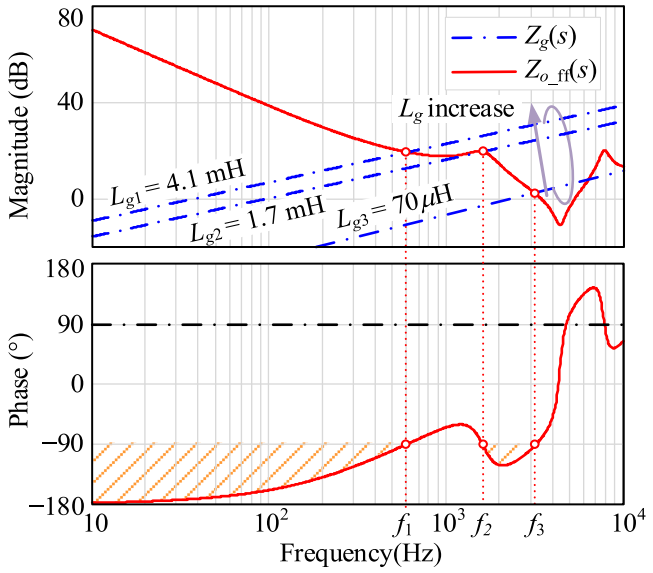

Fig. 3. Bode diagrams of the grid impedance and inverter output impedances with full-feedforward scheme.

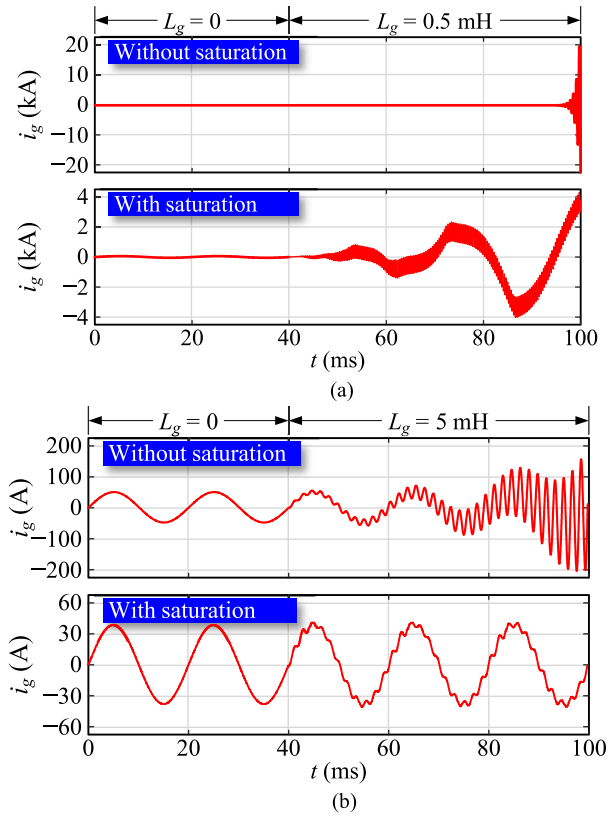

Fig. 4. Simulation results when the grid inductance L_g is plugged in (a) L_g = 0.5 mH and (b) L_g = 5 mH.

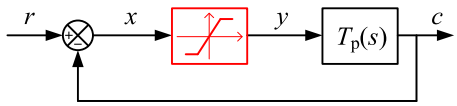

Fig. 5. General block diagram of the saturated system.

the inverter cannot stably operate. Substituting the boundary frequencies f_1, f_2, and f_3 into (3), and letting $|Z_o| = |Z_g|$, yields the corresponding critical values of the grid inductance, i.e., $L_{g1} \approx 4.1$ mH, $L_{g2} \approx 1.7$ mH, and $L_{g3} \approx 70$ μH, respectively. It implies when the grid inductance $L_g \in [L_{g3}, L_{g2}]$ or $L_g > L_{g1}$, the undesired instability would occur. According to the linear control theory, i_g should *diverge*.

B. Instability Behavior With Controller Saturation

To examine the above theoretical analysis, two examples under the assumption of $L_g = 0.5$ mH ($L_g \in [L_{g3}, L_{g2}]$) and $L_g = 5$ mH ($L_g > L_{g1}$) are given. The simulation was conducted via the block diagram shown in Fig. 2(a). Fig. 4 shows the simulation results where comparisons are provided to unfold the effect of the controller saturation. Here, the controller parameters in $G_i(s)$ and K_d keep the same as given in Table I. The limits of the controller saturation equal the peak values of the carrier and the grid inductance is plugged in at $t = 40$ ms.

Fig. 4(a) shows the simulation results under $L_g = 0.5$ mH. As shown, no matter the controller saturation is considered or not, the grid current i_g ultimately diverges, meaning the inverter is unstable. The result agrees with the above theoretical expectation.

However, it can be found that the controller saturation actually affects the divergence speed. Fig. 4(b) shows the simulation results under $L_g = 5$ mH. As shown, when the controller saturation is not considered, i_g is divergent, in agreement with the theoretical expectation. However, when the saturation is considered, i_g is convergent and a critically stable operation with constant-amplitude oscillation is presented, which does not agree with the above analysis.

Above comparisons confirm that the controller saturation indeed poses great impact on the instability behavior. Yet, its mechanism remains unclear, although this phenomenon has ever been reported in the previous pieces of literature.

IV. Impact Mechanism of Controller Saturation on Instability Behavior

Describing function is an effective tool to analyze the nonlinear system. In this section, the proper describing function for describing the controller saturation will be derived, and its impact mechanism on the instability behavior is elaborated based on the generalized Nyquist stability criterion.

A. Basis of Controller Saturation

Fig. 5 shows the block diagram of a universal feedback control system, where $T_p(s)$ represents the loop gain of the linear part of the plant, r and c represent the input and output signals of the system, respectively, and x and y represent the input and output signals of the controller saturation, respectively. The relation of x and y is depicted in Fig. 6, where $\pm D$ are the limits of the

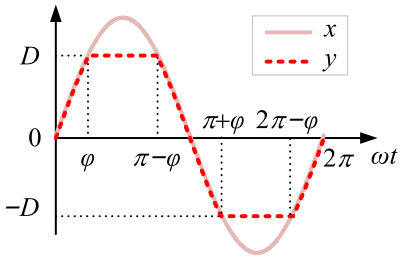

Fig. 6. Relation of x and y.

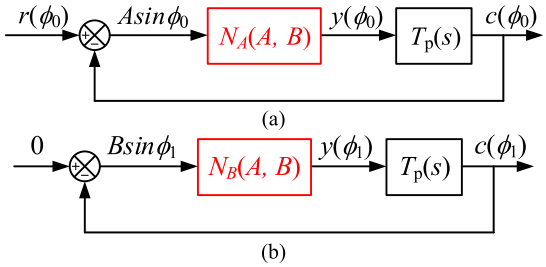

Fig. 7. Form of the nonlinear system in charge of (a) fundamental component and (b) harmonic component.

controller saturation. When x exceeds $\pm D$, y would be limited to $\pm D$; otherwise, y equals x.

As for the grid-connected inverter, the input signal x is actually the modulation signal v_{M} (see Fig. 1), which should stay within the limits of the controller saturation when the inverter is stable. Accordingly, x mainly contains the fundamental component and is sinusoidal in the steady state. However, when instability occurs, x will be distorted by the harmonics from the feedback of the unstable grid current i_g, and thus tend to exceed the limits of the controller saturation. According to Fig. 6, the output of the controller saturation, i.e., y in the positive half cycle can be expressed as

$$y(t) = \begin{cases} x(t) & \omega t \in [0, \varphi] \cup [\pi - \varphi, \pi] \\ D & \omega t \in (\varphi, \pi - \varphi) \end{cases} \tag{11}$$

where φ is the phase in corresponding to $x = D$.

B. Describing Function of Controller Saturation

For the purpose of describing function calculation, the nonlinear input signal x of the saturation can be expressed as [37]

$$x(t) = A \sin \omega_0 t + B \sin(\omega_1 t + \delta) \tag{12}$$

where ω_0 and ω_1 represent the fundamental and the harmonic frequencies, respectively; A and B are their corresponding amplitudes; δ is the initial phase of the harmonic. For convenience, $\phi_0 = \omega_0 t$ and $\phi_1 = \omega_1 t + \delta$ are defined.

Recalling that y is a periodic function, its Fourier series expansion can be derived as

$$\begin{aligned} y(x) &= y(A \sin \phi_0 + B \sin \phi_1) \\ &= \sum_{\mathrm{m}=0}^{\infty} \sum_{\substack{n=-\infty(m\neq 0) \\ n=0(m=0)}}^{\infty} [P_{mn} \sin(m\phi_0 + n\phi_1) \\ &\quad + Q_{mn} \cos(m\phi_0 + n\phi_1)] \end{aligned} \tag{13}$$

where m and n are integers. The Fourier coefficients P_{mn} and Q_{mn} can be calculated as

$$\begin{aligned} P_{mn} &= \frac{1}{2\pi^2} \int_{-\pi}^{\pi} \int_{-\pi}^{\pi} y(A \sin \phi_0 + B \sin \phi_1) \\ &\quad \times \sin(m\phi_0 + n\phi_1)\, d\phi_0 d\phi_1 \\ Q_{mn} &= \frac{1}{2\pi^2} \int_{-\pi}^{\pi} \int_{-\pi}^{\pi} y(A \sin \phi_0 + B \sin \phi_1) \\ &\quad \times \cos(m\phi_0 + n\phi_1)\, d\phi_0 d\phi_1. \end{aligned} \tag{14}$$

Since the controller saturation is odd, $Q_{mn} = 0$ holds. Besides, thanks to the existence of the output low-pass *LCL* filter, it is valid to only concern the fundamental component ($m = 1$, $n = 0$) and the first-order harmonic component ($m = 0, n = 1$) in (13) [37]. Accordingly, two Fourier coefficients P_{10} and P_{01} can be separately calculated and two associated describing functions for the controller saturation are

$$N_A(A, B) = P_{10}/A \tag{15}$$

$$N_B(A, B) = P_{10}/B \tag{16}$$

where $N_A(A, B)$ and $N_B(A, B)$ are in charge of the fundamental component and the first-order harmonic component, respectively. The derivation of $N_A(A, B)$ and $N_B(A, B)$ is given in the appendix and expressed as (A5) and (A6), respectively.

Based on the above analysis, Fig. 5 can be decomposed into Fig. 7(a) and (b), to separately illustrate the generation of the fundamental component and the harmonic component in y, respectively. When the system turns to be unstable, the harmonic amplitude B increases. Thus, it is reasonable to use Fig. 7(b) and the associated describing function $N_B(A, B)$ to assess the impact mechanism of the controller saturation on the system instability phenomenon.

C. Impact Mechanism on Instability Behavior

According to Fig. 7(b), the system characteristic equation can be derived as

$$1 + N_B(A, B) T_p(s) = 0. \tag{17}$$

As known, in the classic linear control theory, the characteristic equation is $1 + T_p(s) = 0$, excluding $N_B(A, B)$, and the associated Nyquist stability criterion regards $(-1, j0)$ as the critical point for stability assessment. However, (17) implies that, when the controller saturation is considered, the critical point $(-1, j0)$ should be changed to $(-1/N_B(A, B), j0)$ while keeping the Nyquist contour of $T_p(j\omega)$ unchanged. This is recognized as the generalized Nyquist stability criterion.

As can be observed from (A6) in the Appendix, $N_B(A, B)$ is the function of the fundamental amplitude A and harmonic amplitude B. As the oscillation grows, B increases and thus $N_B(A, B)$ shifts. Accordingly, $-1/N_B(A, B)$ is a line rather than a point, as shown in Fig. 8, where its arrow direction denotes the increment of B. Thus, the system stability will dynamically vary, depending on the variation of B. For better clarify, the Nyquist contour of $T_p(j\omega)$ is also depicted in Fig. 8. The arrow direction

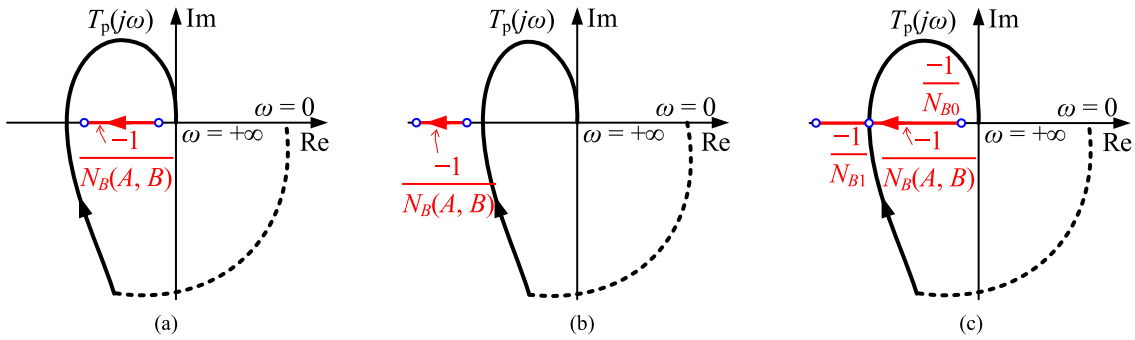

Fig. 8. Relations of $T_p(j\omega)$ and $-1/N_B(A, B)$. (a) $-1/N_B(A, B)$ is encircled by $T_p(j\omega)$. (b) $-1/N_B(A, B)$ is not encircled by $T_p(j\omega)$. (c) $-1/N_B(A, B)$ is partly encircled by $T_p(j\omega)$ and $-1/N_{B0} > -1/N_{B1}$ holds.

of its Nyquist contour denotes the increment of ω. According to the relation of $T_p(j\omega)$ and $-1/N_B(A, B)$, two cases can be classified and the impact mechanism of the controller saturation on the instability behavior can be interpreted as follows:

1) No Intersection Between $T_p(j\omega)$ and $-1/N_B(A, B)$: In this case, $-1/N_B(A, B)$ may be encircled by $T_p(j\omega)$ [see Fig. 8(a)] or not [see Fig. 8(b)]. Define N as the number of clockwise encirclements of the critical point by $T_p(j\omega)$ from $\omega = 0$ to $\omega = +\infty$. As for the former, there is a clockwise encirclement of $(-1/N_B(A, B), j0)$, i.e., $N = 1$. As for the latter, there is no encirclement of $(-1/N_B(A, B), j0)$, i.e., $N = 0$. According to the Nyquist stability criterion, $P = 2N$ should be satisfied for the stable operation where P is the number of the open-loop right-half-plane (RHP) pole. Assuming a minimum- phase system is examined, i.e., $P = 0$, the associated case in Fig. 8(a) is unstable, whereas the one in Fig. 8(b) is stable.

2) Existing Intersection Between $T_p(j\omega)$ and $-1/N_B(A, B)$: In this case, $-1/N_B(A, B)$ is partly encircled by $T_p(j\omega)$ [see Fig. 8(c)]. Assume $-1/N_{B0}$ is the initial point of the line $-1/N_B(A, B)$, and $-1/N_{B1}$ is the intersection of $T_p(j\omega)$ and $-1/N_B(A, B)$. At the initial operation point, a clockwise encirclement of $(-1/N_B(A, B), j0)$ occurs, i.e., $N = 1$. Provided $P = 0$ still, instability will occur, and thus B increases, leading the operation point to depart from $-1/N_{B0}$ toward $-1/N_{B2}$. Inevitably, it will cross over $-1/N_{B1}$, leading to $N = 0$, and then the system tends to become stable. Then, the amplitude of $N_B(A, B)$ decreases in turn, and the operation point goes back toward $-1/N_{B1}$. Iteratively, the operation point will finally stay at $-1/N_{B1}$ in the steady state, just like the waveform with the controller saturation shown in Fig. 4(b).

The dynamic behaviors discussed above answer why the instability oscillation diverges in some cases but converges or persists for hours in some other cases.

D. Determination of Oscillation Frequency and Amplitude

The oscillation frequency and amplitude can be predicted from the intersection point of $T_p(j\omega)$ and $-1/N_B(A, B)$. The oscillation frequency, denoted as f_B, equals the corresponding frequency of T_p at the intersection point, which can be read from the Nyquist plot. The oscillation amplitude, denoted as I_B, can be obtained by solving the corresponding B in $-1/N_B(A, B)$ at the intersection point, where

$$-\frac{1}{N_B(A, B)} = T_p(j \cdot 2\pi f_B). \tag{18}$$

In order to solve the two unknowns A and B in (18), another relation is established based on Fig. 7(a) in the following. Considering that the fundamental component $c(\phi_0)$ can still track the given current reference $r(\phi_0)$ in this case [see Fig. 4(b)], there exists

$$c(\phi_0) = A \sin\phi_0 \cdot N_A(A, B) \cdot T_p(j\omega_0) \approx r(\phi_0). \tag{19}$$

Combining (18) and (19), and substituting (A5) and (A6) into them, the values of A and B could be solved numerically. Referring to the general model shown in Fig. 7(b), the value of B corresponds to the oscillation amplitude I_B.

V. Case Study in the Grid-Connected Inverter

In this section, a normalized model of the grid-connected inverter (similar to Fig. 5) is developed, and the impact of the controller saturation on its instability behavior is thoroughly studied.

A. Normalized Model

Via series of equivalent transformations, Fig. 2(a) is normalized into Fig. 9(c). The transformation process includes the following three steps.

1) The grid voltage v_g shown in Fig. 2(a), as an independent variable, is regarded as a disturbance and omitted in the stability analysis and the grid impedance $Z_g = sL_g$ is considered here, giving Fig. 9(a).
2) Changing the feedback variable from i_C to i_g, and adjusting the associated feedback gain, yields Fig. 9(b).
3) Moving the feedback node of i_g from the input of $G_i(s)$ to its output, Fig. 9(b) can be further arranged as Fig. 9(c), where G_{x1} and G_{x2} are

$$G_{x1}(s) = \frac{G_d(s)}{s^3 L_1 (L_2 + L_g) C + s(L_1 + L_2 + L_g)} \tag{20}$$

$$G_{x2}(s) = G_i(s) + s^2 K_d (L_2 + L_g) C - sL_g G_{ff}(s). \tag{21}$$

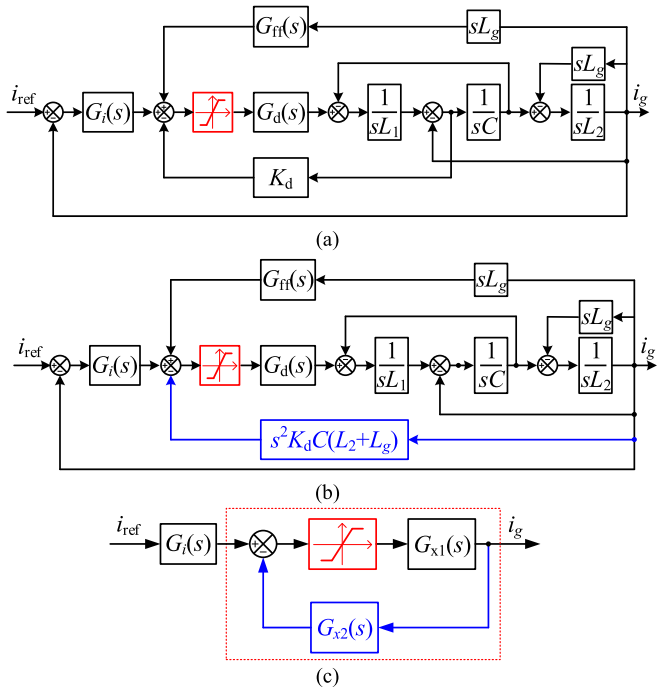

Fig. 9. Equivalent transformations of Fig. 2(a).

Accordingly, the loop gain of the linear part in the dash block in Fig. 9(c), denoted by $T_p(s)$, can be derived as

$$T_p(s) = G_{x1}(s)\,G_{x2}(s) = \frac{G_i(s) + s^2K_dC(L_2+L_g) - sL_gG_{ff}(s)}{s^3L_1(L_2+L_g)C + s(L_1+L_2+L_g)}G_d(s). \quad (22)$$

B. Stability Assessment

For the grid-connected inverter with the PCC voltage feedforward, the non-minimum phase behavior may happen, which fortunately can be avoided by properly designing the controller parameters [38]. Referring to [38] and according to the main parameters given in Table I, the controller parameters were designed which ensure a minimum phase behavior for the system. Accordingly, there is no RHP pole in T_p. Meanwhile, $N_B(A, B)$ does not provide the RHP pole either. Thus, the number of the open-loop RHP pole is zero, i.e., $P = 0$. According to the generalized Nyquist stability criterion, the number of clockwise encirclements must be zero (i.e., $N = 0$) to ensure the system stability. On this basis, identical with Fig. 4, the stability of the grid-connected inverter under $L_g = 0$ mH, $L_g = 0.5$ mH, and $L_g = 5$ mH are sequentially studied.

According to (22) and (A6), the Nyquist contours of $T_p(j\omega)$ and the lines $-1/N_B(A, B)$ under these three grid impedances are depicted, as shown in Fig. 10(a)–(c), respectively. At the initial instant, the input signal of the controller saturation does not exceed the limits $\pm D$. In this case, its output equals the input, which indicates $N_B(A, B) = 1$. Accordingly, the lines $-1/N_B(A, B)$ all start from the point $(-1, j0)$ in these figures. According to (A6), the value of $N_B(A, B)$ is a real number and decreases as B increases. Therefore, with the increase of B, the lines of $-1/N_B(A, B)$ gradually move towards the negative infinity along the negative real axis, whereas the Nyquist contours of $T_p(j\omega)$ show different characteristics.

Referring to Fig. 8, the system stability in the three cases can be interpreted as follows.

1) $L_g = 0$ mH [see Fig. 10(a)]: There is no encirclement of $(-1/N_B(A, B), j0)$ like Fig. 8(b), resulting in $N = 0$. Thus, the system must be stable.

2) $L_g = 0.5$ mH [see Fig. 10(b)]: Initially, $-1/N_B(A, B)$ locates at $(-1, j0)$ and a clockwise encirclement of $(-1/N_B(A, B), j0)$ occurs, i.e., $N = 1$, leading to instability. Accordingly, the amplitude of the harmonic component, i.e., B, increases, which makes the operation point of $-1/N_B(A, B)$ move to the left of $(-1, j0)$.

Nevertheless, $(-1/N_B(A, B), j0)$ is always encircled by $T_p(j\omega)$ in the clockwise direction like Fig. 8(a). That is, $N = 1$ always holds. Thus, the amplitude of harmonic component will continuously increase, until triggers the system protection.

3) $L_g = 5$ mH [see Fig. 10(c)]: Initially, $-1/N_B(A, B)$ also locates at $(-1, j0)$, and two clockwise and one anti-clockwise encirclements of $(-1/N_B(A, B), j0)$ occur, resulting in $N = 1$. Likewise, instability occurs, B increases and the operation point of $-1/N_B(A, B)$ moves to the left of $(-1, j0)$ accordingly. Interestingly, once it passes point K_1 which is measured as (–1.015, 0), the encirclement number changes, since there only leaves one clockwise and one anticlockwise encirclements, resulting in $N = 0$. Thereby, the system returns to be stable and thus the harmonic component decays (i.e., B decreases). Accordingly, $-1/N_B(A, B)$ moves back toward $(-1, j0)$. Iteratively, $-1/N_B(A, B)$ will ultimately stay at K_1, which features a stable operation with the constant-amplitude oscillation. This case is similar to Fig. 8(c). Following the procedure described in Section IV-D, the oscillation frequency f_B and amplitude I_B can be predicted. Specifically, f_B equals the frequency of the Nyquist contour approaching K_1, yielding $f_B = 560$ Hz. Substituting f_B into (18) and combining with (19), $B = 0.375$ can be solved. It is worth noting that different with the general model shown in Fig. 7(b), the feedback gain in Fig. 9(c) is not unity and thus the oscillation amplitude is expressed as $I_B = B{\cdot}N_B(A,B){\cdot}|G_{x1}(j2\pi f_B)|$. With $B = 0.375$, $N_B(A, B) = -1/1.015$ and $f_B = 560$ Hz, we have $I_B = 3.2$ A.

The above conclusions match well with the simulation results shown in Fig. 4. Most of importance, the above analysis well explained why the system presents a different response, and clearly illustrated how the controller saturation affects the system instability behavior.

C. Oscillation Frequency Shift

It is worth noting that the controller saturation also shifts the oscillation frequency a little. When the controller saturation is not considered, the system stability is usually predicted by the classic Nyquist stability criterion. According to Fig. 2(a), the system loop gain without considering the saturation is derived and its Nyquist contour under $L_g = 5$ mH is plotted, as shown in Fig. 11. As can be observed, only one clockwise encirclement

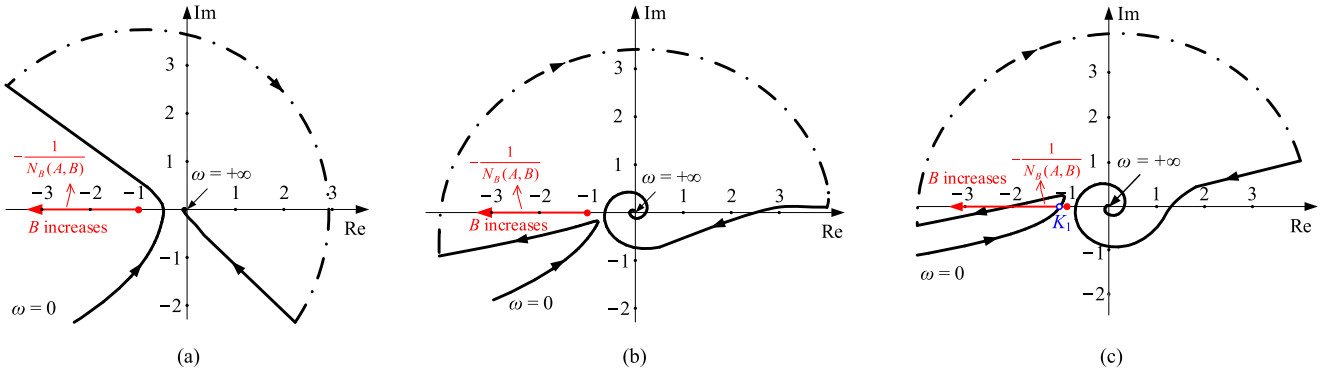

Fig. 10. Nyquist plots of $T_p(j\omega)$ and $-1/N_B(A, B)$. (a) $L_g = 0$ mH. (b) $L_g = 0.5$ mH. (c) $L_g = 5$ mH.

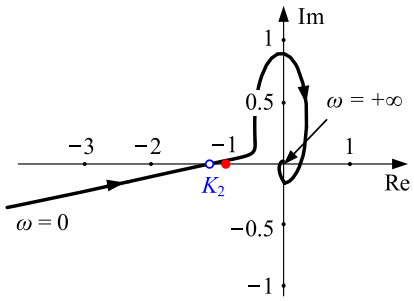

Fig. 11. Nyquist plot of the system without considering the controller saturation under $L_g = 5$ mH.

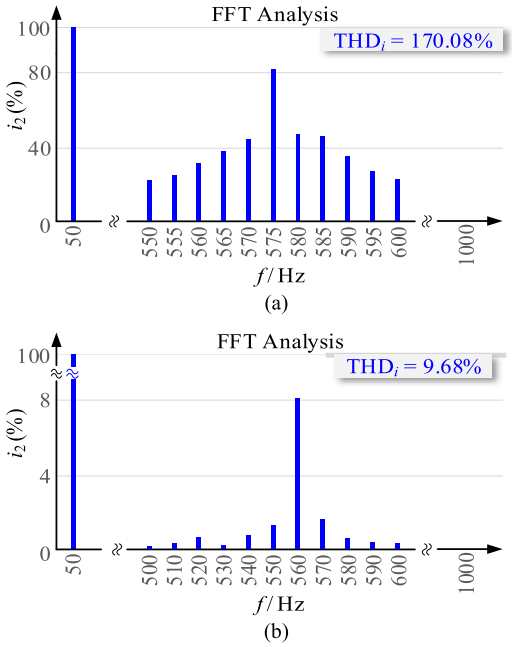

Fig. 12. FFT analysis results of the grid current under $L_g = 5$ mH. (a) Without controller saturation. (b) With controller saturation.

of $(-1, j0)$ occurs, i.e., $N = 1$, resulting in instability. The oscillation frequency is the frequency of the Nyquist contour approaching K_2, which is 575 Hz. Compared with the one with controller saturation (i.e., 560 Hz), the oscillation frequency changes a little.

The simulation results under $L_g = 5$ mH have been presented in Fig. 4(b), and the relevant fast Fourier transform (FFT) analysis of the grid current is supplemented here, as shown in Fig. 12. When the controller saturation is not considered, the oscillation frequency is around 575 Hz [see Fig. 12(a)]; In contrast, when the controller saturation is considered, the dominant oscillation frequency is 560 Hz and the corresponding oscillation amplitude is measured as 3.16A [see Fig. 12(b)]. The simulation results agree with the theoretical analysis.

VI. Experimental Verification

To verify the correctness of the above theoretical analysis, a 6-kW single-phase *LCL*-type grid-connected inverter was built and tested in the lab. The configuration of the experimental setup is shown in Fig. 13, and the main parameters of the prototype are given in Table I. The control algorithm is implemented in a TI TMS320F2812 DSP. The current transducer LA-55P and voltage transducer LV-25P are used to acquire the current and voltage signals, respectively. The grid is emulated by a Chroma 6590 programmable AC source and an external inductor. The Oscilloscope (LeCroy 44Xi-A) is used to record the experimental results.

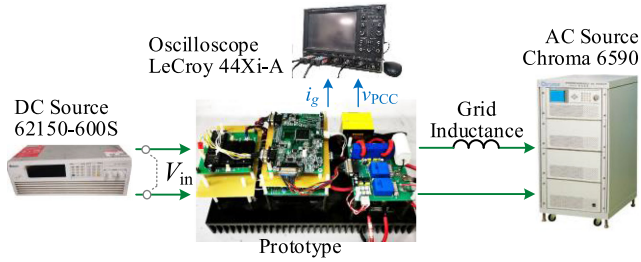

Fig. 13. Configuration of the experimental setup.

The first set of experiments were conducted under $L_g = 0$ mH. Comparative experiments without and with the PCC voltage feedforward scheme are conducted, and the results are shown in Fig. 14. Without the feedforward, i_g is distorted due to the background harmonics in v_{PCC}, as shown in Fig. 14(a), where

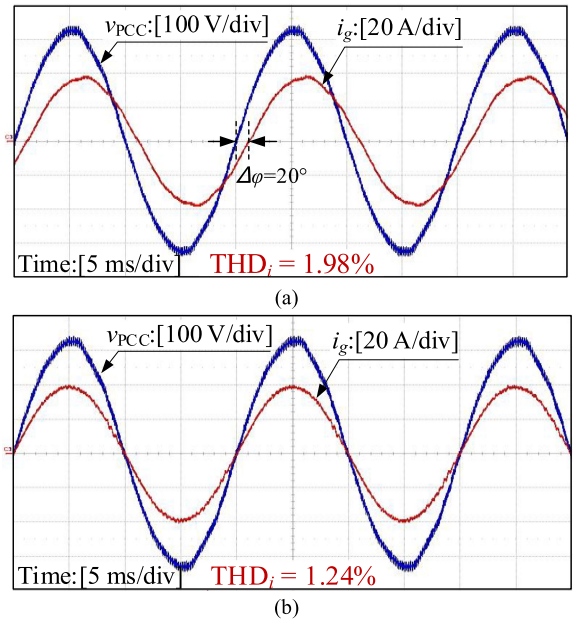

Fig. 14. Experimental results of the grid-connected inverter under $L_g = 0$ mH. (a) Without PCC voltage full-feedforward scheme. (b) With PCC voltage full -feedforward scheme.

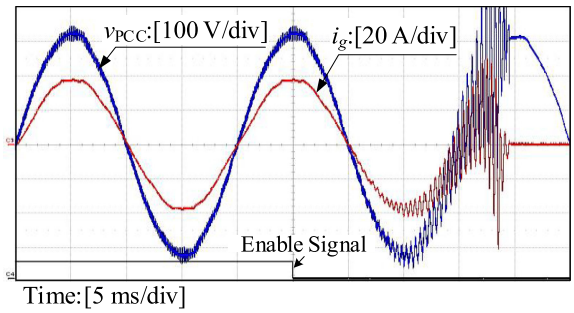

Fig. 15. Experimental results of the grid-connected inverter under $L_g = 0.5$ mH.

the measured total harmonic distortion (THD) of i_g is 1.98%. Moreover, i_g lags behind $v_{\rm PCC}$ with a phase of 20°, which is resulted from the fundamental component of $v_{\rm PCC}$. In contrast, with the PCC voltage feedforward, i_g becomes sinusoidal, as shown in Fig. 14(b), the measured THD is reduced to 1.24%, and the phase lag between i_g and $v_{\rm PCC}$ is eliminated. The results verified the necessity of the PCC voltage feedforward scheme, and confirmed that the system is stable under $L_g = 0$ mH.

The second set of experiment was conducted to examine the response of the grid-connected inverter under $L_g = 0.5$ mH. The experimental result is shown in Fig. 15. Here, in order to capture the divergent waveform, the control algorithm is intentionally altered from a weighted proportional PCC voltage feedforward scheme [39] (the weighted coefficient is 0.6) to the PCC voltage full-feedforward scheme at the falling edge of the enable signal. As can be observed, the system is initially stable, and the associated waveform of the grid current i_g is less sinusoidal than that in Fig. 14(b). When the full-feedforward scheme is

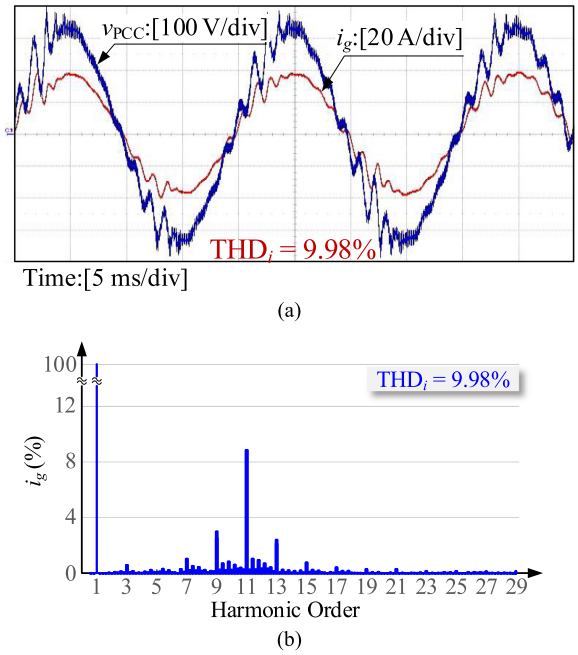

Fig. 16. Experimental results of the grid-connected inverter with the PCC voltage full-feedforward scheme under $L_g = 5$ mH. (a) Waveforms. (b) FFT analysis of the grid current.

enabled, severe oscillation arises in i_g and tends to diverge, which ultimately triggers protection. This is in agreement with the analysis in Section V.

The third set of experiment was conducted to examine the response under $L_g = 5$ mH. Fig. 16 gives the experimental results with the PCC voltage full-feedforward scheme. As shown in Fig. 16(a), noticeable oscillation still arises but the oscillation does not diverge. This result matches well with the analysis in Section V-B. Besides, the relevant harmonic spectrum is shown in Fig. 16(b). As shown, the measured THD of i_g is 9.9%, the dominant components are located around the 11th harmonics with the frequency near 560 Hz and the amplitude of 3.3 A. This coincides well with the theoretical expectation.

The above experimental results are consistent with the simulation results shown in Fig. 4 and verified the correctness of the theoretical analysis, and the impact of the controller saturation on the system stability behavior is confirmed.

VII. Conclusion

This article studied the impact mechanism of the controller saturation on the instability behavior of grid-connected inverters. A linear model including the controller saturation was derived, and the impact mechanism of the controller saturation on the system stability was unfolded. It is revealed that the controller saturation essentially causes the system operation point to drift. In some cases, this process will eventually bring the system to a critically stable operation, leading to the sustained oscillation. From this point, this article fills the void in explaining why some negative-damped resonances in conventional stability analysis behave as constant-amplitude oscillations rather than divergent

oscillations in practice. The above findings have been verified by the simulation and experimental results.

APPENDIX

In this appendix, the expressions of $N_A(A, B)$ and $N_B(A, B)$ are derived.

According to (14), the integral should be performed. Referring to Fig. 6, the integral area can be divided into three parts σ_1, σ_2 and σ_3, i.e.,

$$\begin{aligned}&\sigma_1 : A\sin\phi_0 + B\sin\phi_1 > D\\&\sigma_2 : A\sin\phi_0 + B\sin\phi_1 < -D\\&\sigma_3 : -D \le A\sin\phi_0 + B\sin\phi_1 \le D.\end{aligned} \tag{A1}$$

Taking P_{10} as an example, the integral therein is shown as step 1 in (A2) shown at bottom of this page. Then, considering the integral of $(A\sin\phi_0 + B\sin\phi_1)\sin\phi_0$ in the whole integral area $\sigma_1 + \sigma_2 + \sigma_3$ is $2\pi^2 A$, step 2 in (A2) is yielded. Unfortunately, the integral operation regarding ϕ_0 is actually an elliptic integral which can hardly be executed in practice. To address this issue, the fourth-order Newton–Cotes formula is applied for the approximation calculation [40], yielding STEP 3 in (A2) where

$$\begin{aligned}f_1(x) = {} & (D - B\cos x)\sqrt{1 - \left(\frac{D - B\cos x}{A}\right)^2}\\ & - A\cos^{-1}\frac{D - B\cos x}{A}\end{aligned} \tag{A3}$$

$$b_1 = \cos^{-1}\left(\frac{D - A}{B}\right). \tag{A4}$$

Substituting (A2) into (15), yields

$$N_A(A, B) = \frac{b_1}{45\pi^2 A}\begin{bmatrix}7f_1(0) + 32f_1\left(\frac{b_1}{4}\right) + 12f_1\left(\frac{b_1}{2}\right)\\ +32f_1\left(\frac{3b_1}{4}\right) + 7f_1(b_1)\end{bmatrix} + 1. \tag{A5}$$

Likewise, the expression of $N_B(A, B)$ can be derived as

$$N_B(A, B) = \frac{b_2}{45\pi^2 B}\begin{bmatrix}7f_2(0) + 32f_2\left(\frac{b_2}{4}\right) + 12f_2\left(\frac{b_2}{2}\right)\\ +32f_2\left(\frac{3b_2}{4}\right) + 7f_2(b_2)\end{bmatrix} + 1 \tag{A6}$$

where

$$\begin{aligned}f_2(x) = {} & (D - A\cos x)\sqrt{1 - \left(\frac{D - A\cos x}{B}\right)^2}\\ & - B\cos^{-1}\frac{D - A\cos x}{B}\end{aligned} \tag{A7}$$

$$b_2 = \cos^{-1}\left(\frac{D - B}{A}\right). \tag{A8}$$

REFERENCES

[1] B. Kroposki *et al.*, "Achieving a 100% renewable grid: Operating electric power systems with extremely high levels of variable renewable energy," *IEEE Power Energy Mag.,* vol. 15, no. 2, pp. 61–73, Mar./Apr. 2017.

[2] F. Blaabjerg, R. Teodorescu, M. Liserre, and A. V. Timbus, "Overview of control and grid synchronization for distributed power generation systems," *IEEE Trans. Ind. Electron.*, vol. 53, no. 5, pp. 1398–1409, Oct. 2006.

[3] Q. Liu, T. Caldognetto, and S. Buso, "Review and comparison of grid-tied inverter controllers in microgrids," *IEEE Trans. Power Electron.*, vol. 35, no. 7, pp. 7624–7639, Jul. 2020.

[4] X. Ruan, X. Wang, D. Pan, D. Yang, W. Li, and C. Bao, *Control Techniques for LCL-Type Grid-Connected Inverters*. Singapore: Springer, 2017.

[5] Q. Peng, Q. Jiang, Y. Yang, T. Liu, H. Wang, and F. Blaabjerg, "On the stability of power electronics-dominated systems: Challenges and potential solutions," *IEEE Trans. Ind. Appl.*, vol. 55, no. 6, pp. 7657–7670, Nov./Dec. 2019.

[6] J. H. R. Enslin and P. J. M. Heskes, "Harmonic interaction between a large number of distributed power inverters and the distribution network," *IEEE Trans. Power Electron.*, vol. 19, no. 6, pp. 1586–1593, Nov. 2004.

[7] C. Buchhagen, M. Greve, A. Menze, and J. Jung, "Harmonic stability — Practical experience of a TSO," in *Proc. Wind Intergr. Workshop*, Nov. 2016, pp. 1–6.

[8] M. Amin and M. Molinas, "Understanding the origin of oscillatory phenomena observed between wind farms and HVDC systems," *IEEE J. Emerg. Sel. Topics Power Electron.*, vol. 5, no. 1, pp. 378–392, Mar. 2017.

[9] C. Li, "Unstable operation of photovoltaic inverter from field experiences," *IEEE Trans. Power Del.*, vol. 33, no. 2, pp. 1013–1015, Apr. 2018.

[10] E. Mollerstedt and B. Bernhardsson, "Out of control because of harmonics—An analysis of the harmonic response of an inverter locomotive," *IEEE Control Syst. Mag.*, vol. 20, no. 4, pp. 70–81, Aug. 2000.

[11] C. Buchhagen, C. Rauscher, A. Menze, and J. Jung, "BorWin1—First experiences with harmonic interactions in converter dominated grids," in *Proc. Int. ETG Congr., Die Energiewende — Blueprints New Energy Age*, Nov. 2015, pp. 1–7.

[12] C. Zou *et al.*, "Analysis of resonance between a VSC-HVDC converter and the AC grid," *IEEE Trans. Power Electron.*, vol. 33, no. 12, pp. 10157–10168, Dec. 2018.

[13] J. Sun, G. Wang, X. Du, and H. Wang, "A theory for harmonics created by resonance in converter-grid systems," *IEEE Trans. Power Electron.*, vol. 34, no. 4, pp. 3025–3029, Apr. 2019.

[14] X. Wang, F. Blaabjerg, and W. Wu, "Modeling and analysis of harmonic stability in an AC power-electronics-based power system," *IEEE Trans. Power Electron.*, vol. 29, no. 12, pp. 6421–6432, Dec. 2014.

$$\begin{aligned}P_{10} &= \frac{1}{2\pi^2}\int_{-\pi}^{\pi}\int_{-\pi}^{\pi} y\,(A\sin\phi_0 + B\sin\phi_1)\sin\phi_0 d\phi_0 d\phi_1\\ &= \frac{1}{2\pi^2}\left[\oint\oint_{\sigma_1} D\sin\phi_0 d\sigma + \oint\oint_{\sigma_2}(-D)\sin\phi_0 d\sigma + \oint\oint_{\sigma_3}(A\sin\phi_0 + B\sin\phi_1)\sin\phi_0 d\sigma\right] && \text{(Step 1)}\\ &= \frac{2}{\pi^2}\int_0^{\cos^{-1}\frac{D-A}{B}}\left((D - B\cos\phi_0)\sqrt{1 - \left(\frac{D - B\cos\phi_0}{A}\right)^2} - A\cos^{-1}\left(\frac{D - B\cos\phi_0}{A}\right)\right)d\phi_1 + A && \text{(Step 2)}\\ &\approx \frac{b_1}{45\pi^2}\left[7f_1(0) + 32f_1\left(\frac{b}{4}\right) + 12f_1\left(\frac{b}{2}\right) + 32f_1\left(\frac{3b}{4}\right) + 7f_1(b)\right] + A && \text{(Step 3)}\end{aligned} \tag{A2}$$

[15] X. Wang and F. Blaabjerg, "Harmonic stability in power electronic based power systems: Concept, modeling, and analysis," *IEEE Trans. Smart Grid*, vol. 10, no. 3, pp. 2858–2870, May 2019.
[16] D. Yang, X. Wang, and F. Blaabjerg, "Sideband harmonic instability of paralleled inverters with asynchronous carriers," *IEEE Trans. Power Electron.*, vol. 33, no. 6, pp. 4571–4577, Jun. 2018.
[17] L. Harnefors, X. Wang, A. G. Yepes, and F. Blaabjerg, "Passivity-based stability assessment of grid-connected VSCs — An overview," *IEEE J. Emerg. Sel. Topics Power Electron.*, vol. 4, no. 1, pp. 116–125, Mar. 2016.
[18] Y. Liao and X. Wang, "Impedance-based stability analysis for interconnected converter systems with open-loop RHP poles," *IEEE Trans. Power Electron.*, vol. 35, no. 4, pp. 4388–4397, Apr. 2020.
[19] M. Amin and M. Molinas, "Small-signal stability assessment of power electronics based power systems: A discussion of impedance- and eigenvalue-based methods," *IEEE Trans. Ind. Appl.*, vol. 53, no. 5, pp. 5014–5030, Sep./Oct. 2017.
[20] P. Kundur. *Power System Stability and Control*. New York, NY, USA: McGraw-Hill, 1994.
[21] J. Sun, "Small-signal methods for AC distributed power systems — A review," *IEEE Trans. Power Electron.*, vol. 24, no. 11, pp. 2545–2554, Nov. 2009.
[22] J. Sun, "Impedance-based stability criterion for grid-connected inverters," *IEEE Trans. Power Electron.*, vol. 26, no. 11, pp. 3075–3078, Nov. 2011.
[23] D. Yang, X. Ruan, and H. Wu, "Impedance shaping of the grid- connected inverter with *LCL* filter to improve its adaptability to the weak grid condition," *IEEE Trans. Power Electron.*, vol. 29, no. 11, pp. 5795–5805, Nov. 2014.
[24] A. Rygg, M. Molinas, C. Zhang, and X. Cai, "A modified sequence-domain impedance definition and its equivalence to the *dq*-domain impedance definition for the stability analysis of AC power electronic systems," *IEEE Trans. Emerg. Sel. Topics Power Electron.*, vol. 4, no. 4, pp. 1383–1396, Dec. 2016.
[25] J. Xu, S. Xie, B. Zhang, and Q. Qian, "Robust grid current control with impedance-phase shaping for *LCL*-filtered inverters in weak and distorted grid," *IEEE Trans. Power Electron.*, vol. 33, no. 12, pp. 10240–10250, Dec. 2018.
[26] G. C. Goodwin, S. F. Graebe, and M. E. Salgado, *Control System Design*. Upper Saddle River, NJ, USA: Prentice-Hall, 2000.
[27] P. T. Krein and R. M. Bass, "Multiple limit cycle phenomena in switching power converters," in *Proc. 4th Annu. IEEE Appl. Power Electron. Conf. Expo*., Mar. 1989, pp. 143–148.
[28] H. Zhang, X. Yang, X. Ma, and B. He, "Analysis of limit cycle behavior in dc-dc boost converters," *Nonlinear Anal. Real World Appl.*, vol. 13, pp. 2049–2062, Oct. 2012.
[29] D. Pan, X. Ruan, X. Wang, H. Yu, and Z. Xing, "Analysis and design of current control schemes for *LCL*-type grid-connected inverter based on a general mathematical model," *IEEE Trans. Power Electron.*, vol. 32, no. 6, pp. 4395–4410, Jun. 2017.
[30] O. R. Fendrich, "Describing functions and limit cycles," *IEEE Trans. Automat. Control*, vol. 37, no. 4, pp. 486–487, Apr. 1992.
[31] S. C. Chung, S. R. Huang, and E. C. Lee, "Applications of describing functions to estimate the performance of nonlinear inductance," *Proc. Inst. Elect. Eng. Sci., Meas. Technol.*, vol. 48, no. 3, pp. 108–114, May 2001.
[32] R. A. Mastromauro, M. Liserre, and A. D. Aquila, "Study of the effects of inductor nonlinear behavior on the performance of current controller for single-phase PV grid converters," *IEEE Trans. Ind. Electron.*, vol. 55, no. 5, pp. 2043–2052, May 2008.
[33] W. Wei, Y. Xia, and F. Blaabjerg, "Nonlinear stability analysis for three-phase grid-connected PV generators," *IEEE J. Emerg. Sel. Topics Power Electron.*, vol. 8, no. 4, pp. 3487–3501, Sep. 2019.
[34] M. Berg and T. Roinila, "Nonlinear effect of deadtime in small-signal modeling of power-electronics system under low load conditions," *IEEE J. Emerg. Sel. Topics Power Electron.*, vol. 8, no. 4, pp. 3204–3213, Jan. 2020.
[35] X. Wang, X. Ruan, S. Liu, and C. K. Tse, "Full feedforward of grid voltage for grid-connected inverter with *LCL* filter to suppress current distortion due to grid voltage harmonics," *IEEE Trans. Power Electron.*, vol. 25, no. 12, pp. 3119–3127, Dec. 2010.
[36] D. Pan, X. Ruan, and X. Wang, "Direct realization of digital differentiators in discrete domain for active damping of *LCL*-type grid-connected inverter," *IEEE Trans. Power Electron.*, vol. 33, no. 10, pp. 8461–8473, Oct. 2018.
[37] A. Gelb and W. E. V. Velde, *Multiple-Input Describing Functions and Nonlinear System Design*. New York, NY, USA: McGraw-Hill, 1968.
[38] Y. He, X. Wang, X. Ruan, D. Pan, and K. Qin, "Hybrid active damping combining capacitor current feedback and point of common coupling voltage feedforward for *LCL*-type grid-connected inverter," *IEEE Trans. Power Electron.*, vol. 36, no. 2, pp. 2373–2383, Feb. 2021.
[39] Q. Qian, S. Xie, L. Huang, J. Xu, Z. Zhang, and B. Zhang, "Harmonic suppression and stability enhancement for parallel multiple grid-connected inverters based on passive inverter output impedance," *IEEE Trans. Ind. Electron.*, vol. 64, no. 9, pp. 7587–7598, Sep. 2017.
[40] Z. Kalogiratou and T. E. Simos, "Newton–Cotes formulae for long-time integration," *J. Comput. Appl. Math.*, vol. 158, no. 1, pp. 75–82, 2003.

Xuehua Wang (Member, IEEE) received the B.S. degree from the Nanjing University of Technology, Nanjing, China, in 2001, and the M.S. and Ph.D. degrees from the Nanjing University of Aeronautics and Astronautics, Nanjing, China, in 2004 and 2008, respectively, all in electrical engineering.

Since 2008, he has been with the Huazhong University of Science and Technology, Wuhan, China, where he was a Postdoctoral Fellow, from 2008 to 2011, and is an Associate Professor with the School of Electrical and Electronic Engineering. His main research interests include multilevel inverter and renewable energy generation system.

Yuying He (Member, IEEE) received the B.S. degree in electrical engineering from Central South University, Changsha, China, in 2015. She is currently working toward the Ph.D. degree in electrical engineering with the Huazhong University of Science and Technology, Wuhan, China.

Since May 2021, she has been a Visiting Researcher with E.ON Energy Research Center, RWTH Aachen University, Aachen, Germany. Her research interests include modeling and control of grid-connected converters, harmonics analysis and control, and stability of renewable energy generation system.

Kuang Qin received the B.S. and M.S. degrees in electrical engineering from the Huazhong University of Science and Technology, Wuhan, China, in 2017 and 2020, respectively.

He is currently with State Grid Hunan Electric Power Company Limited Economic and Technical Research Institute, Changsha, China. His research interests include control of grid-connected converters under weak grid condition, and renewable energy generation system.

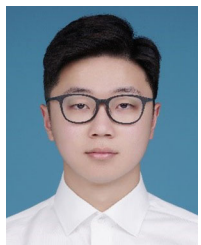

Hao Zhang (Student Member, IEEE) received the B.S. degree in electrical engineering from Chongqing University, Chongqing, China, in 2020. He is currently working toward the M.S. degree in electrical engineering with the Huazhong University of Science and Technology, Wuhan, China.

His research interests include modeling and control of grid-connected converters, harmonics analysis and control, and stability of renewable energy generation system.

Donghua Pan (Member, IEEE) received the B.S. and Ph.D. degrees in electrical engineering from the Huazhong University of Science and Technology, Wuhan, China, in 2010 and 2015, respectively.

From July 2015 to August 2017, he was a Research Engineer with Inovance Technology Company, Ltd., Suzhou, China. From September 2017 to October 2019, he was a Postdoctoral Fellow with the Department of Energy Technology, Aalborg University, Aalborg, Denmark. Since November 2019, he has been a Senior Manager with a holding company of China State Shipbuilding Corporation, Wuhan, China. He has authored or coauthored more than 40 peer-reviewed technical papers and a book *Control Techniques for LCL-type Grid-connected Inverters* (Springer, 2018). His research interests include magnetic integration techniques, modeling and control of grid-connected converters, and wide bandgap power conversion systems.

Dr. Pan was the recipient of the 2017 Outstanding Reviewer Award for the IEEE TRANSACTIONS ON POWER ELECTRONICS, the Best Paper Award at IEEE SPEC 2018, and the World's Top 2% Scientists 2020 by Stanford University.

Xinbo Ruan (Fellow, IEEE) received the B.S. and Ph.D. degrees in electrical engineering from the Nanjing University of Aeronautics and Astronautics (NUAA), Nanjing, China, in 1991 and 1996, respectively.

In 1996, he was with the Faculty of Electrical Engineering Teaching and Research Division, NUAA, where he was a Professor with the College of Automation Engineering in 2002. From August to October 2007, he was a Research Fellow with the Department of Electronic and Information Engineering, Hong Kong Polytechnic University, Hong Kong. From March 2008 to August 2011, he was with the School of Electrical and Electronic Engineering, Huazhong University of Science and Technology, Wuhan, China. He is the author or co-author of 11 books and more than 300 technical papers published in journals and conferences. His main research interests include soft-switching dc–dc converters, soft-switching inverters, power factor correction converters, modeling the converters, power electronics system integration and renewable energy generation system.

Dr. Ruan was a recipient of the Delta Scholarship by the Delta Environment and Education Fund in 2003 and was a recipient of the Special Appointed Professor of the Chang Jiang Scholars Program by the Ministry of Education, China, in 2007. From 2005 to 2013, and since 2017 again, he was the Vice President of the China Power Supply Society, and since 2008, he has been a member of the Technical Committee on Renewable Energy Systems within the IEEE Industrial Electronics Society. He is currently an Editor for the IEEE JOURNAL OF EMERGING AND SELECTED TOPICS ON POWER ELECTRONICS and an Associate Editor for the IEEE TRANSACTIONS ON INDUSTRIAL ELECTRONICS, IEEE TRANSACTIONS ON POWER ELECTRONICS, IEEE OPEN JOURNAL OF INDUSTRIAL ELECTRONICS SOCIETY, and IEEE TRANSACTIONS ON CIRCUITS AND SYSTEMS – II: EXPRESS BRIEFS.

Qingfeng Zhou received the B.S. and M.S. degrees in electrical engineering from the Huazhong University of Science and Technology, Wuhan, China, in 2015 and 2018, respectively.

He is currently an Electrical Engineer with NR Electric Company, Ltd, Nanjing, China. His current research interests include modeling and control of grid-connected converters and renewable energy generation system.

Chuan Yao was born in Jiangxi Province, China, in 1986. He received the B.S. degree in the electrical engineering and automatization from Chongqing University, Chongqing, China, in 2007, and the Ph.D. degree in electrical engineering from the Huazhong University of Science and Technology, Wuhan, China, in 2013.

He is currently with the Wuhan Second Ship Design and Research Institute, Wuhan, China. His main research interests include design and control of power converter, battery management system, and renewable energy generation system.